

Article

Mesoporous Chromium Catalysts Templated on Halloysite Nanotubes and Aluminosilicate Core/Shell Composites for Oxidative Dehydrogenation of Propane with CO₂

Dmitry Melnikov^{1,*}, Ekaterina Smirnova¹, Marina Reshetina¹, Andrei Novikov¹ , Hongqiang Wang², Evgenii Ivanov¹ , Vladimir Vinokurov¹  and Aleksandr Glotov^{1,*} 

¹ Physical and Colloid Chemistry Department, Faculty of Chemical and Environmental Engineering, National University of Oil and Gas (Gubkin University), 65 Leninsky Prospekt, Moscow 119991, Russia; smirnova.em94@gmail.com (E.S.); reshetina.mv@yandex.ru (M.R.); ivanov166@list.ru (E.I.)

² State Key Laboratory of Solidification Processing, Center for Nano Energy Materials, School of Materials Science and Engineering, Northwestern Polytechnical University and Shaanxi Joint Laboratory of Graphene (NPU), No. 127, Youyi West Road, Xi'an 710072, China; hongqiang.wang@nwpu.edu.cn

* Correspondence: melnikov.dp@mail.ru (D.M.); glotov.a@gubkin.ru (A.G.)

Abstract: The oxidative dehydrogenation of alkanes is a prospective method for olefins production. CO₂-assisted propane dehydrogenation over metal oxide catalysts provides an opportunity to increase propylene production with collateral CO₂ utilization. We prepared the chromia catalysts on various mesoporous aluminosilicate supports, such as halloysite nanotubes, nanostructured core/shell composites of MCM-41/halloysite (halloysite nanotubes for the core; silica of MCM-41-type for the shell), and MCM-41@halloysite (silica of MCM-41-type for the core; halloysite nanotubes for the shell). The catalysts have been characterized by X-ray fluorescence analysis, low-temperature nitrogen adsorption, X-ray diffraction, temperature-programmed reduction, temperature-programmed desorption of ammonia, transmission electron microscopy with energy-dispersive X-ray spectroscopy, and thermogravimetric analysis. The catalysts' performance in carbon-dioxide-assisted propane dehydrogenation has been estimated in a fixed-bed reactor at atmospheric pressure. The most stable catalyst is Cr/halloysite, having the lowest activity and the largest pore diameter. The catalyst, Cr/MCM-41/HNT, shows the best catalytic performance: having the highest conversion (19–88%), selectivity (83–30%), and space–time yield (4.3–7.1 mol C₃H₆/kg catalyst/h) at the temperature range of 550–700 °C. The highest space–time yield could be related to the uniform distribution of the chromia particles over the large surface area and narrow pore size distribution of 2–4 nm provided by the MCM-41-type silica and transport channels of 12–15 nm from the halloysite nanotubes.

Keywords: propylene; aluminosilicate; nanotubes; oxidative dehydrogenation; mesoporous materials; mesoporous silica



Citation: Melnikov, D.; Smirnova, E.; Reshetina, M.; Novikov, A.; Wang, H.; Ivanov, E.; Vinokurov, V.; Glotov, A. Mesoporous Chromium Catalysts Templated on Halloysite Nanotubes and Aluminosilicate Core/Shell Composites for Oxidative Dehydrogenation of Propane with CO₂. *Catalysts* **2023**, *13*, 882. <https://doi.org/10.3390/catal13050882>

Academic Editors: Lei Liu and Zhijun Zuo

Received: 7 April 2023

Revised: 10 May 2023

Accepted: 11 May 2023

Published: 13 May 2023



Copyright: © 2023 by the authors. Licensee MDPI, Basel, Switzerland. This article is an open access article distributed under the terms and conditions of the Creative Commons Attribution (CC BY) license (<https://creativecommons.org/licenses/by/4.0/>).

1. Introduction

Olefins are the basis of the modern petrochemical industry. The production of most bulk polymers is based on olefins polymerization. Many other petrochemical products are also olefin derivatives. Ethylene is the leading olefin, with an annual production exceeding 200 million metric tons, and is mainly used for the production of polyethylene, ethylene dichloride, ethylbenzene, and ethylene oxide. Propylene is the second largest-scale olefin, with an annual production of over 100 million metric tons. Polypropylene, acrylonitrile, propylene oxide, isopropyl benzene, and oxo alcohols are among the main products of propylene conversion [1–3].

While steam cracking is the exclusive method of ethylene production almost used, the main processes of propylene production are the steam cracking of hydrocarbons, fluid catalytic cracking (FCC), and propane dehydrogenation. Other processes, such as olefin

metathesis and methanol-to-propylene, make no significant contribution to gross propylene production [4].

Typically, the propylene yield is two times lower than that of ethylene in the steam cracking of C_{4+} hydrocarbons [5], while propylene demand is not significantly lower. As a result, this causes the so-called propylene gap between its demand and supply. The main product of FCC is gasoline; therefore, this process is not the solution to the problem. Choosing a catalyst with higher olefin yields could contribute to propylene production, yet it will not change the main product.

To overcome the propylene gap, neither steam cracking nor FCC can be used, as the main product of these is ethylene and gasoline, correspondingly. The most suitable method for on-purpose propylene production is propane dehydrogenation [6].

Only dehydrogenation processes allow on-purpose propylene production, which is important to overcome when considering the propylene gap between propylene production and demand [3,7]. Moreover, the shale gas revolution and widespread liquefied natural gas (LNG) technologies have increased the production of light alkanes, especially propane, and increased interest in alkane dehydrogenation as a way of natural gas liquids utilization [6]. The typical propylene yield from propane is 2.5–3 times lower compared to that of ethylene [5,8]; thus, the conversion of light alkanes in steam cracking even increases the propylene gap.

The dehydrogenation of alkanes can be performed in two principal ways: non-oxidative dehydrogenation or oxidative dehydrogenation [6]. The dehydrogenation thermodynamics requires high temperatures, which leads to increased by-product formation at high conversion rates. To achieve an acceptable propane conversion, temperatures above 550 °C and low pressures are required [9]. The oxidative process facilitates hydrogen removal and benefits the propylene yield but also increases undesirable deep oxidation.

Only a few processes have been implemented on an industrial scale: Oleflex by UOP, Catofin by Lummus, K-PRO by KBR, and STAR by ThyssenKrupp [6,7,10]. The first three processes are non-oxidative ones, and only the last one includes a partial oxidation step. The Oleflex process is based on UOP's continuous catalytic reforming technology and uses similar platinum-based catalysts with a tin addition, and is potassium-promoted. This is the most widely used propane dehydrogenation process worldwide [4]. Catofin is a mature technology based on a short-cycle dehydrogenation process and uses a chromia-based catalyst that is promoted with alkali. K-PRO is a modification of KBR's well-established and widely used fluid catalytic cracking technology, Orthoflow [4]. The catalyst is proprietary and undisclosed, but it is chromia and platinum-free. The STAR process is based on classical steam/secondary methane reforming [10]. The feature of the STAR process is the oxidative second stage at which oxygen is added to burn H_2 and increases the equilibrium propylene yield. As the last reaction is highly exothermic, the overall process is also exothermic. The catalyst is platinum-based with the addition of Sn.

Oxidative dehydrogenation can be performed using various oxidants: O_2 , N_2O , or CO_2 [11,12]. Oxygen decreases significantly at an operating temperature and removes coke, but it can also lead to deep oxidation. Moreover, oxygen production is highly energy-consuming. N_2O is toxic, and its production is also energy-consuming. Carbon dioxide is interesting for two reasons. CO_2 is a mild oxidant, which is favorable for the propylene yield. Additionally, CO_2 utilization is important for the sustainability of the petrochemical industry [9,13], where its chemical usage instead of release to the atmosphere is one of the most prospective utilization ways. Produced CO can be used for downstream petrochemical processes, such as oxo alcohols and Fischer–Tropsch synthesis.

Typical active components of non-oxidative dehydrogenation catalysts are platinum or metal oxides, such as chromia, vanadia, and molybdena [6]. In oxidative propane dehydrogenation, Pt-based catalysts are active in dry propane reforming, thus resulting in low selectivity to propylene [9]. Transition metal oxides are preferably active components for this process, facilitating the Mars–van Krevelen mechanism [14,15]. Chromia catalysts are among the most investigated in oxidative dehydrogenation [16–19]. CO_2 , as an oxidant,

removes hydrogen from the active sites by the reverse water–gas shift reaction but is unable to oxidize chromium to the inactive states Cr^{5+} and Cr^{6+} [6]. Other widely investigated active components are the oxides of molybdenum, vanadium, and gallium [20–24].

Typical supports for the dehydrogenation catalysts are SiO_2 and Al_2O_3 [22,25–28]. Along with the traditional supports, such as alumina and silica, ordered mesoporous silica [29–32] and zeolites [33,34] are also an object of interest. Both types of materials have a well-defined structure with narrow pore size distributions and high surface areas. The chemical nature of ordered mesoporous silicas provides excellent thermal stability [35]. The acidity of silica is lower than that of zeolites, which favors high selectivity in alkane dehydrogenation [36]. In contrast, the high acidity of zeolites prevents their direct use as dehydrogenation catalysts and demands careful dealumination to ensure high selectivity to olefins [37].

Various types of mesoporous silicas are also widely investigated as supports for dehydrogenation catalysts [29,38–44]. It was shown that a high surface area of mesoporous silica favors the formation of sub-nanosized particles of the active phase of dehydrogenation catalysts [45]. Low loadings of chromium in SBA-1 lead to a high abundance of Cr^{5+} species [29]. A comparison of SBA-15 as the catalyst support with Al_2O_3 and ZrO_2 shows benefits for both oxidative and non-oxidative propane dehydrogenation [40]. Nevertheless, mesoporous silicas show the partial collapse of their structure during dehydrogenation [44]. Recently, mesoporous organo-silica has been investigated as a support of CO_2 -assisted ethane dehydrogenation [46]. Mesoporous silica was doped with $\text{Ce}_x\text{Zr}_{1-x}\text{O}_2$ to promote oxygen mobility [47].

Halloysite is a mesoporous aluminosilicate comprising kaolin sheets rolled into nanotubes with a non-uniform charge distribution [48]. The nanotubes have a typical external diameter of 40–50 nm, a lumen internal diameter of 10–15 nm, and a length of up to 1500 nm [49]. Halloysite demonstrates excellent mechanical properties and may serve as a reinforcing additive to paper [50], polymer scaffolds [51], and silica gels for water shutoff [52]. The lumen of the nanotubes can be loaded with functional materials, ensuring their controlled release over usage time and, therefore, providing the deacidification of paper [50], as well as corrosion-inhibiting [53] and antibacterial properties [54]. The internal “alumina” surface is positively charged, whereas the outside “silica” surface has a negative charge. Thereby, halloysite tubes can be modified in various ways: acid or alkali etching and grafting with silanes and azines [55–59]. Interestingly, the asymmetry of the charge allows for modifying the exclusively internal or external nanotube surfaces, thus easing the regioselective construction of complicated composites [60] and layer-by-layer self-assembly of nanotubes into structures [61]. Halloysite nanotubes can be used as a reinforcing core for MCM-41 synthesis, thus improving the mechanical properties of the resulting composites [62,63]. Such functional materials have already been investigated in benzene hydrogenation [62] and p-xylene oxidation [64]. Another option is to use halloysite as a shell for the MCM-41 encapsulated inside nanotubes [65].

The present work is devoted to the synthesis and investigation of chromia-based catalysts supported on halloysite and halloysite-derived mesoporous core/shell materials, such as MCM-41/halloysite (halloysite nanotubes for the core; silica of MCM-41-type for the shell), and MCM-41@halloysite (silica of MCM-41-type for the core; halloysite nanotubes for the shell) in the oxidative dehydrogenation of propane, using CO_2 as an oxidant.

2. Results and Discussion

Three functional materials have been investigated in this work: pristine halloysite nanotubes (HNT); MCM-41, synthesized around halloysite (MCM-41/HNT); and MCM-41, synthesized inside the halloysite lumen (MCM-41@HNT). The general idea was to compare these materials’ similarities by composition as catalyst supports and elucidate the influence of their morphology on catalytic performance.

The structure of the synthesized functional materials has been estimated by low-temperature N_2 adsorption (Table 1). Pristine HNT has a BET surface area of $67 \text{ m}^2/\text{g}$, a

pore volume of $0.30 \text{ cm}^3/\text{g}$, and an average pore diameter (D_p) of 14 nm. The MCM-41 synthesis around HNTs increases the BET surface area up to $887 \text{ m}^2/\text{g}$, a pore volume to $0.59 \text{ cm}^3/\text{g}$, and decreases the pore diameter to 3 nm, which is close to the typical value for MCM-41. These dramatic changes are caused by the formation of MCM-41, not only around the nanotubes but also in the standalone phase. The synthesis of MCM-41 inside the halloysite nanotubes increases the BET surface area ($324 \text{ m}^2/\text{g}$) and pore volume ($0.37 \text{ cm}^3/\text{g}$) to a smaller extent due to the restriction of MCM-41 nucleation and decreases the pore diameter less significantly, which could indicate that not all nanotubes are filled with mesoporous silica. In this way, functional materials with high surface areas, low acidity, and high mechanical strength could be prepared based on widely spread natural halloysite clays.

Table 1. Properties of functional materials and catalysts.

Functional Material/Catalyst	$S_{\text{BET}}, \text{m}^2/\text{g}$	Pore Volume *, cm^3/g	Pore Diameter **, nm	Cr content ***, %wt.	Acidity, mmol NH_3/g
HNT	67	0.30	14	-	0.175
MCM-41/HNT	887	0.59	2.5; 14	-	0.326
MCM-41@HNT	324	0.37	2.6; 14	-	0.271
5%Cr/HNT	53	0.29	12	4.4	0.101
5%Cr/MCM-41/HNT	558	0.32	2.4; 12	4.9	0.217
5%Cr/MCM-41@HNT	264	0.32	2.8; 12	4.7	0.180

* BJH method (desorption). ** Two values correspond to the maxima of bimodal distribution. *** XRF data.

We used boehmite as a binder (20 %wt.) for granulating the catalysts, thus mimicking industrial-scale catalyst preparation. The binder simplifies the catalyst handling and its loading into the reactor. However, the addition of the binder may alter the textural properties of the catalyst support and complicate the microscopic assessment of the prepared catalysts. The deposition of the active phase (chrome oxide) is another possible cause for the change in textural properties. Therefore, we studied both the source composites and prepared catalysts by low-temperature nitrogen adsorption.

Table 1 also shows the textural properties and chromium content of the catalysts prepared on the functional materials above. After the preparation of the catalyst supports with boehmite forming and further calcination, the BET surface areas, pore volume, and pore diameters have significantly reduced compared to the corresponding functional materials due to the relatively high content of chromia and functional material dilution with boehmite. The chromium contents are close to the nominal value.

Figure 1 shows the corresponding N_2 adsorption isotherms and pore volume distribution vs. pore diameter for the catalysts. Isotherms of Cr/MCM-41/HNT and Cr/MCM-41@HNT have the typical shape specific to MCM-41 [66,67]. The pore volume distribution of Cr/MCM-41/HNT has two maxima at 2.4 and 12 nm. The first one is sharp and corresponds to the MCM-41 pores, and the second wide one could be attributed to the alumina binder. The pore volume distribution of Cr/MCM-41@HNT also has two maxima at 2.8 and 12 nm, with a similar origin. The pore size distribution of Cr/HNT is wide without a sharp maximum.

The observed pore size distributions suggest a significant increase in the catalyst support porosity with additional sharp maxima in Cr/MCM-41/HNT and Cr/MCM-41@HNT, which did not appear in the pore size distribution of Cr/HNT. This increase implies the possible improvement in the catalytic performance due to the larger surface area and availability of the surface for chromia deposition.

Figure 2 shows the X-ray diffraction (XRD) patterns of the fresh calcined catalysts and pure Cr_2O_3 (JCPDS file #38-1497). The Cr/HNT pattern includes reflections at 2θ equal to 24.5, 33.6, 36.2, 50.2, and 54.9, which are typical for Cr_2O_3 . Based on the main reflection (33.62°), the average particle size of the Cr_2O_3 phase has been estimated as 47 nm, based on the Scherrer equation. The samples of Cr/MCM-41/HNT and Cr/MCM-41@HNT do

not show any reflections assigned to chromia, which can be due to the high dispersion and particle localization inside the hierarchical structure of the MCM-41-containing supports. Similar results have been previously observed for V/MCM-41 catalysts and could be related to the high dispersion of chromia, its amorphous state, or its incorporation in the MCM-41 phase [68]. Typically, the chromia phases appear in the XRD patterns of Cr/MCM-41 catalysts when the Cr content is at least 7–10% wt. [69,70].

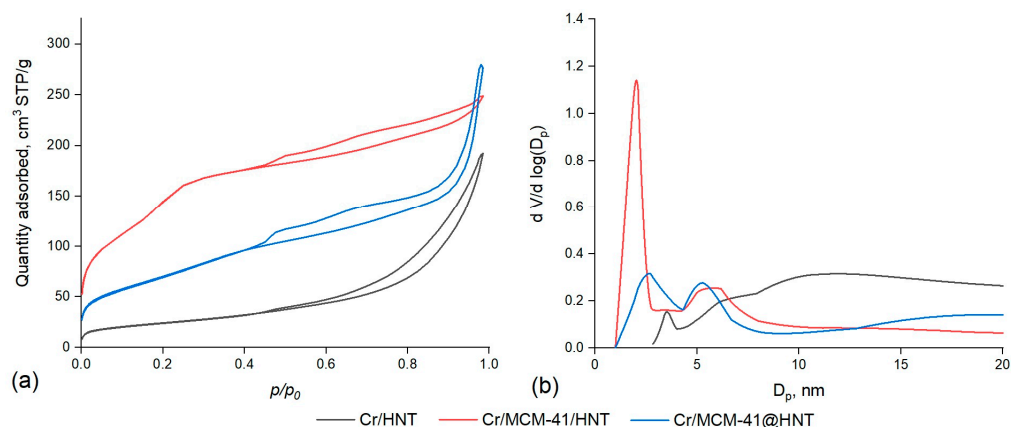


Figure 1. Textural properties of catalysts: (a) Adsorption–desorption isotherms; (b) BJH desorption $dV/d \log(D_p)$ pore size distribution.

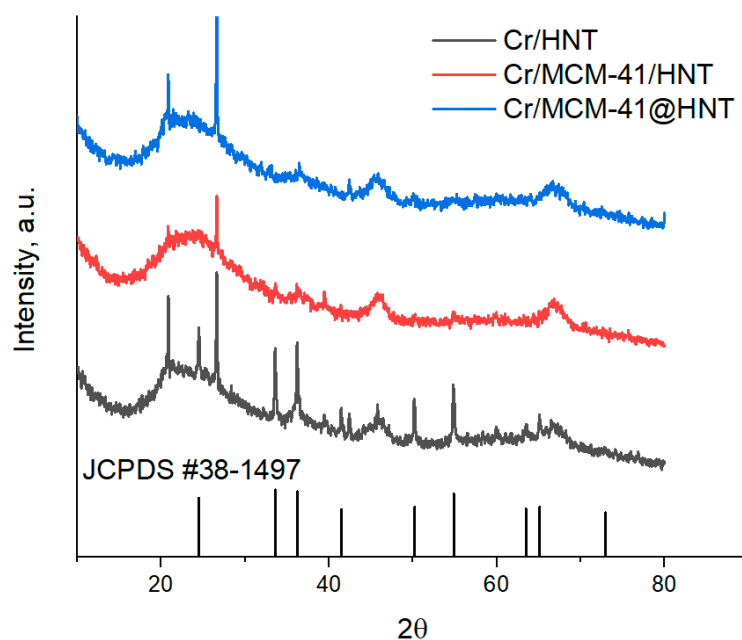


Figure 2. XRD patterns of the catalysts (vertical lines correspond to typical reflections for Cr_2O_3).

Figure 3 shows the TPR- H_2 profiles of the catalysts. Cr/HNT has a reduction peak with a maximum of $\sim 381^\circ\text{C}$, which could be related to the chromate reduction on the “alumina” side of the HNTs [71,72]. Cr/MCM-41@HNT has a peak at 301°C and could be assigned to the chromate reduction over the silica surface. Cr/MCM-41/HNT has a sharp maximum at 295°C and a wide one at 394°C ; therefore, it could be related to both chromates in the MCM-41 pores and lumens of HNTs, correspondingly.

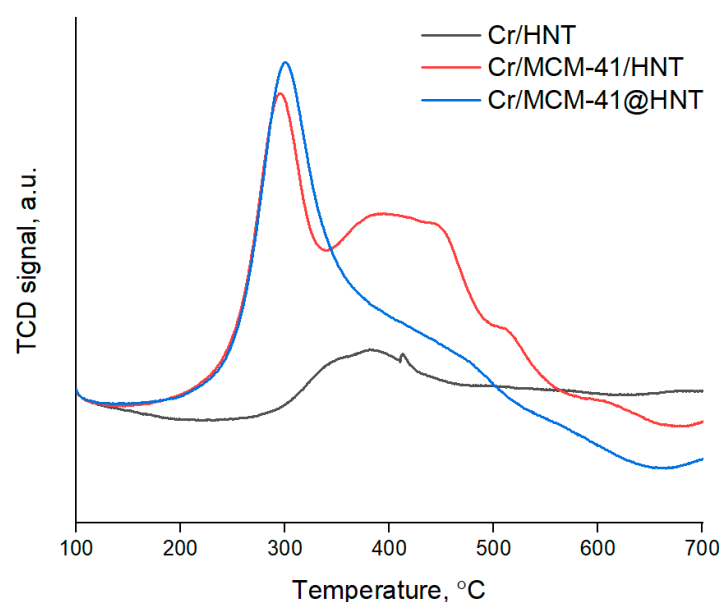


Figure 3. TPR-H₂ profiles of catalysts, black, red, blue.

Figure 4 shows transmission electron microscopy (TEM) images of prepared catalysts. In these TEM micrographs, oblong structures with moderate electron contrast are observed and correspond to halloysite nanotubes. The absence of visible electron-dense particles witnesses that chromia is well-dispersed onto the catalyst support. Cr/HNT catalyst (Figure 4a) shows the typical tubular structure of halloysite nanotubes with some admixture of alumina from the binder. The catalyst Cr/MCM-41/HNT demonstrates the structure of halloysite with MCM-41 material (visible as spongy matter slightly lighter than halloysite) wrapped around, similar to the one reported elsewhere [63]. The catalyst Cr/MCM-41@HNT (Figure 4c) shows silica of MCM-41 type embedded in HNTs without free MCM-41 phase located on its own. TEM results correlate with the low-temperature adsorption data. Particularly, both Cr/MCM-41/HNT and Cr/MCM-41@HNT demonstrate higher BET surface area and maxima in pore size distribution in the 2–3 nm range, explained by the presence of MCM-41-type porous matter.

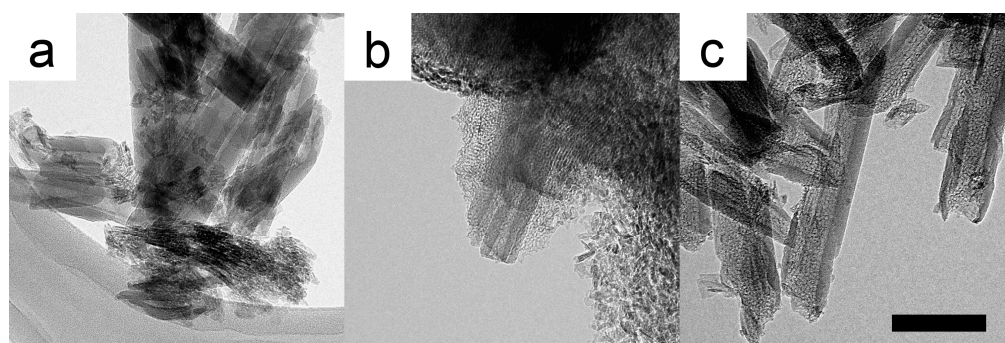


Figure 4. TEM images of catalysts: (a) Cr/HNT; (b) Cr/MCM-41/HNT; (c) Cr/MCM-41@HNT. Scale bar, 100 nm.

The TEM micrographs confirm the expected catalyst morphology: the presence of only tubular structures in Cr/HNT, the simultaneous presence of halloysite nanotubes and mesoporous MCM-41 matter in Cr/MCM-41/HNT, and MCM-41 matter completely packed inside the nanotubes in Cr/MCM-41@HNT. However, the localization of chrome oxide cannot be readily determined by TEM alone. Such an effect could be related to the formation of sub-nanosized particles of the active phase [45].

We performed a detailed STEM/EDX study with elemental mapping to clarify the localization of chromia in the prepared catalysts. Figure 5 shows a bright-field TEM image (a), dark-field STEM micrograph (d), and the corresponding elemental mapping (b,c,e,f) of the same area of the Cr/MCM-41/HNT catalyst. The halloysite nanotube contains aluminum, which is well-defined by the aluminum EDX spectrum (Figure 5e and the blue channel in Figure 5f). Around the nanotube, the MCM-41 framework is formed, which is composed of pure silica, readily visible by its silicon spectrum (Figure 5c and the green channel in Figure 5f). Chromia is uniformly distributed over the catalyst (Figure 5b and the red channel in Figure 5f). The sharp elemental distribution can be observed in the spectral overlay (Figure 5f).

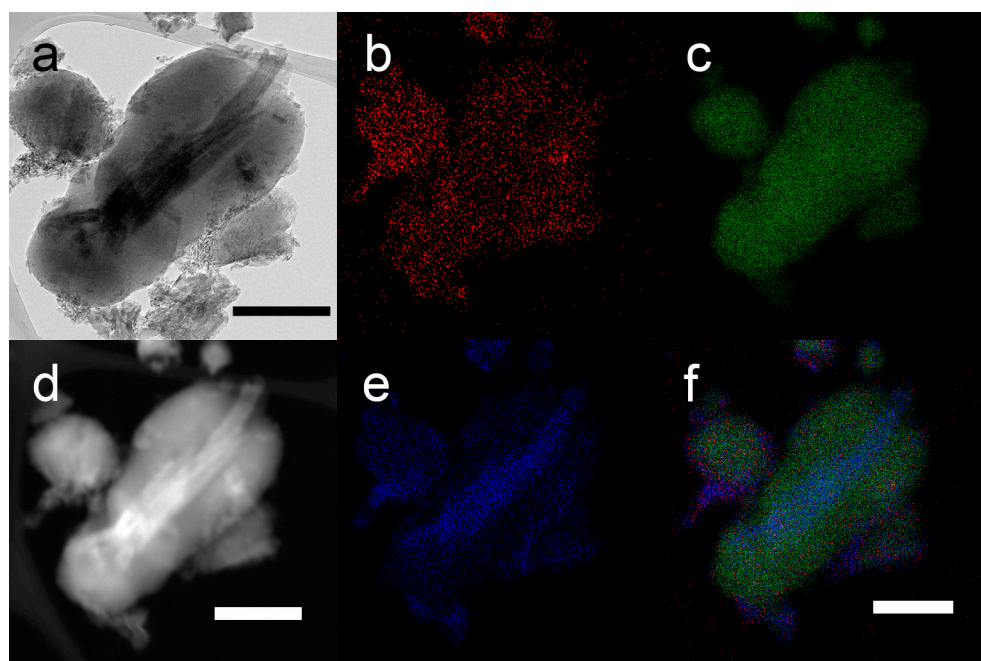


Figure 5. TEM image of Cr/MCM-41/HNT and the corresponding elemental mapping: (a) TEM image; (b) Cr mapping; (c) Si mapping; (d) scanning TEM image; (e) Al mapping; (f) elements overlay. All scale bars, 300 nm.

The STEM/EDX study confirms the structure of the prepared catalysts hypothesized from the TEM images. Particularly, chromia was observed as evenly distributed on the catalyst support surface and not forming separate particles in all the studied samples. The spectral overlay (shown in Figure 5f for the Cr/MCM-41/HNT catalyst) shows the colocalization of Cr with silica (the red and green channels in Figure 5f) or with alumina (the red and blue channels in Figure 5f).

Figure 6 shows the catalytic performance of the samples. The activity of the catalysts could be estimated from the conversion of propane ($X_{C_3H_8}$) vs. temperature dependencies. In the temperature range of 550–700 °C, $X_{C_3H_8}$ over Cr/MCM-/HNT is 0.05–0.15 higher than all the other samples. $X_{C_3H_8}$ over Cr/HNT is the lowest. The selectivity to propylene was also the highest over Cr/MCM-41/HNT, especially at low temperatures. At 550 °C, it was 0.826 compared to 0.756 for Cr/HNT and 0.713 for Cr/MCM-41@HNT. The lowest selectivity was observed over Cr/MCM-41@HNT at any temperature in the investigated range. In terms of the space–time yield (STY), Cr/MCM-41/HNT also demonstrated the highest performance. It increased from 4.3 mol C_3H_6 /kg cat/h at 550 °C to 7.1 mol C_3H_6 /kg cat/h at 700 °C. The STY achieved a maximum at 650 °C for Cr/HNT (5.6 mol C_3H_6 /kg cat/h) and Cr/MCM-41@HNT (5.5 mol C_3H_6 /kg cat/h). The maxima for both samples are due to the selectivity drop while the temperature increases. Figure 6d shows the Arrhenius plots for all the catalysts. The Arrhenius activation energies have

been estimated as 84 ± 6 kJ/mol for Cr/HNT, 66 ± 5 kJ/mol for Cr/MCM-41/HNT, and Cr/MCM-41@HNT for 79 ± 4 kJ/mol. The values are close to the apparent activation energies reported earlier for the Cr/Al₂O₃ catalysts (76–78 kJ/mol) [13] and VO_x/SBA-15 (90 kJ/mol) [73].

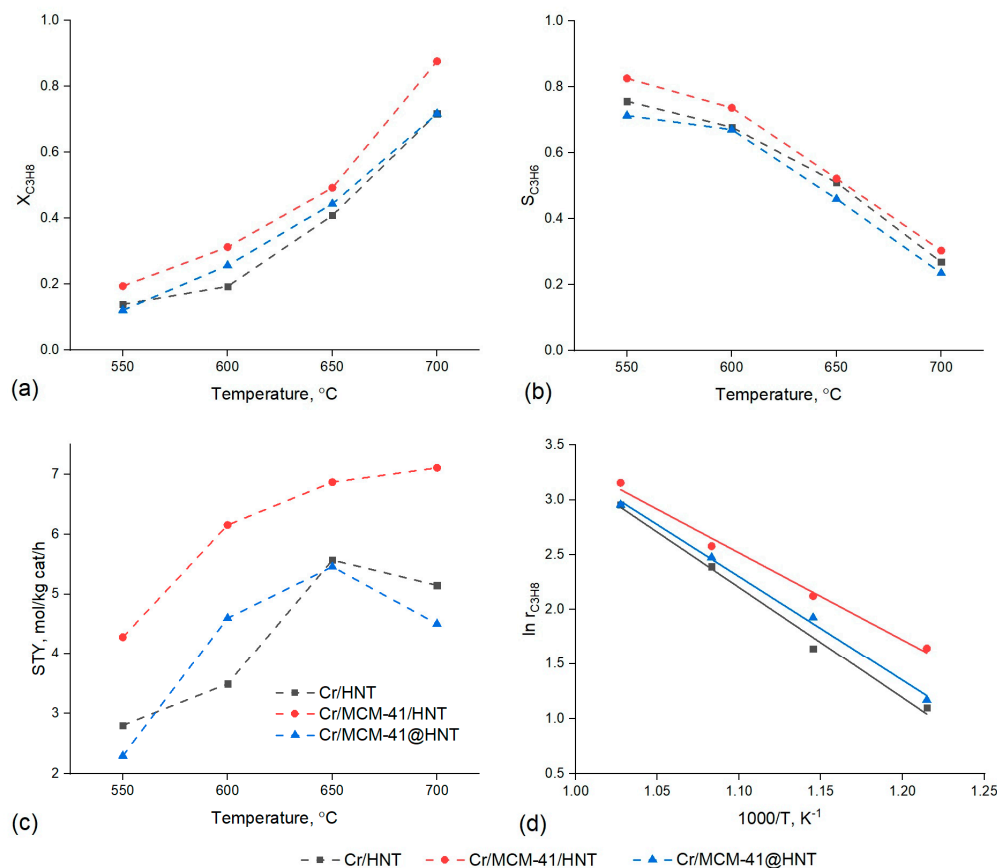


Figure 6. Performance of the catalysts: (a) conversion of propane vs. temperature, (b) selectivity to propylene vs. temperature, (c) space–time yield vs. temperature, (d) Arrhenius plot $\ln r_{C_3H_8} - 1/T$ (dash lines are guides to the eye; solid lines are linear fits; C₃H₈ flow rate is 10 mL/min, molar ratio of CO₂/C₃H₈ = 2, catalyst loading, 1 g).

Table 2 presents more detailed data for the product distribution, as well as the performance of the catalysts in non-oxidative propane dehydrogenation. For the latter experiment, CO₂ was replaced with N₂ to maintain the C₃H₈ partial pressure at the same level. For the experiments without CO₂, one may observe lower propane conversions and higher selectivity to propylene in the same conditions. Meanwhile, the STYs were decreased, indicating lower catalyst (templated on the MCM-41-HNT composites) productivity for propylene for the non-oxidative dehydrogenation process. For the HNT-based sample, the STY values are comparable both for the oxidative and non-oxidative dehydrogenation, which could be ascribed to relatively large polychromate clusters. The same observations were reported by the researchers elsewhere [29].

Figure 7a shows the catalyst stability estimated as the propane conversion drop with the time on stream. The most stable is the Cr/HNT sample, which could be related to the (1) lower activity and the lowest acidity (Table 1), thus, the lower coke formation rate, and (2) the wide pore size of the support (14 nm compared to 2–4 nm for MCM-41/HNT and MCM-41@HNT). The most active and selective catalyst, Cr/MCM-41/HNT, has lower stability, as $X_{C_3H_8}$ decreases from 0.45 to 0.26 in one hour. It can be explained by the higher acidity among all the tested catalysts (0.217 mmol NH₃/g, Table 1), boosting cracking and therefore increasing coke formation. This assumption also agrees with the results obtained

for the Cr/MCM-41@HNT sample. The most stable Cr/HNT catalyst shows the lowest mass loss at 25% wt. Both samples supported on the MCM-41-based composites have a similar mass loss of ca. 46–48% wt (Figure 7b).

Table 2. Catalytic performance of catalysts (C_3H_8 flow rate is 10 mL/min, molar ratio of $CO_2/C_3H_8 = 2$, catalyst loading, 1 g).

Catalyst	T, °C	$\chi_{C_3H_8}$, %	χ_{CO_2} , %	S(H_2), %	Selectivity to Each Component in Hydrocarbon Gases, %					STY, mol/(kg·h)
					CH_4	C_2H_4	C_2H_6	C_3H_6	ΣC_{4+}	
5%Cr/HNT	550	13.8	3.9	1.4	11.4	9.3	3.1	75.6	0.6	2.8
	600	19.3	6.8	2.6	12.5	14.6	4.6	67.7	0.6	3.5
	650	40.8	13.9	5.5	18.5	23.5	5.9	51.0	1.1	5.6
	650 *	33.3	-	7.0	12.4	14.7	7.4	64.7	0.8	5.8
	700	71.7	21.5	9.9	28.6	35.8	6.9	26.9	1.8	5.2
5%Cr/MCM-41/HNT	550	19.4	8.7	3.7	11.1	2.6	3.1	82.6	0.6	4.3
	600	31.2	16.2	6.3	13.2	7.4	4.9	73.7	0.8	6.2
	650	49.2	22.2	11.1	20.8	19.2	6.8	52.2	1.0	6.9
	650 *	38.5	-	10.5	14.8	17.9	6.0	60.4	0.9	6.2
	700	87.6	23.9	13.5	30.4	30.5	7.8	30.3	1.0	7.1
5%Cr/MCM-41@HNT	550	12.0	12.4	1.3	12.5	11.9	3.5	71.3	0.8	2.3
	600	25.6	13.2	4.7	15.5	12.7	4.0	67.0	0.8	4.6
	650	44.3	19.7	9.1	22.3	24.6	6.2	46.0	0.9	5.5
	650 *	27.2	-	8.5	16.1	22.3	4.6	55.0	2.0	4.0
	700	71.7	33.3	14.3	31.4	35.2	8.5	23.5	1.4	4.5

* Dehydrogenation without CO_2 (replaced with N_2 to maintain C_3H_8 partial pressure).

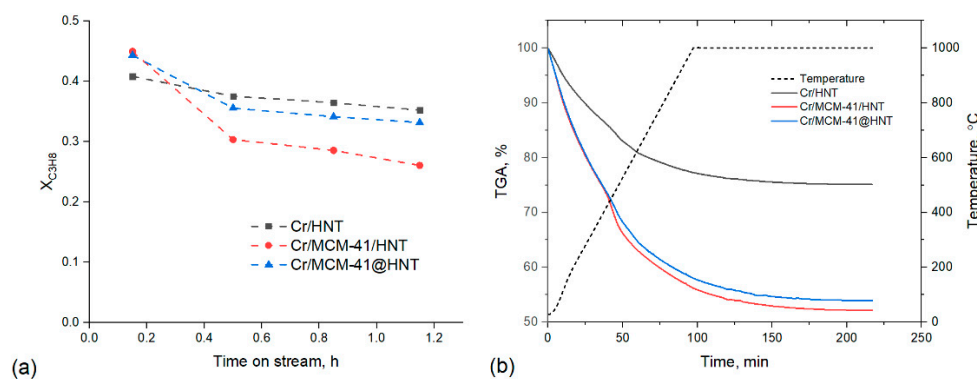


Figure 7. Catalysts stability: (a) conversion vs. time on stream at 650 °C (C_3H_8 flow rate is 10 mL/min, CO_2/C_3H_8 , catalyst loading, 1 g) (dash lines are guides to the eye), and (b) TGA of the spent samples.

It can be concluded that, from the prepared catalysts, Cr/MCM-41/HNT has the highest performance in terms of activity, selectivity, and space–time yield. The use of such materials with high surface areas and hierarchical structures allows for preparing active and selective dehydrogenation catalysts.

3. Materials and Methods

3.1. Materials

The following chemicals have been used for the synthesis of the catalysts: chromium (III) nitrate nonahydrate ($\geq 98\%$, Sigma-Aldrich, St. Louis, MI, USA), halloysite nanoclay ($\geq 98\%$, Sigma-Aldrich, St. Louis, MI, USA), hexadecyltrimethylammonium bromide ($\geq 98\%$, Sigma-Aldrich, St. Louis, MI, USA), tetraethyl orthosilicate ($\geq 98\%$, Sigma-Aldrich, St. Louis, MI, USA), boehmite (Pural SB, Sasol, Hamburg, Germany), aqueous ammonia ($\sim 25\%$, ECOS-1, Moscow, Russia), propanol-2 (ECOS-1, Moscow, Russia), hydrochloric acid

(36.5%, Sigma Tek, Moscow, Russia), and deionized water. Propane and CO₂ were supplied by NIIKM (Moscow, Russia).

3.2. Synthesis of Functional Materials

The ordered functional material MCM-41/HNT, where the MCM-41 was synthesized around halloysite nanotubes, was prepared by a modification of the procedure described in [74]. In a polypropylene flask, a charge of halloysite clay (1.44 g) was dispersed in water (384 mL) by continuous stirring for 1 hour. After that, hexadecyltrimethylammonium bromide (2.00 g), propanol-2 (107.32 g), and aqueous ammonia (35.8 g) were added and stirred for an additional 1 hour. After the addition of tetraethyl orthosilicate (7.48 g), the mixture was stirred for 4 hours. Then, the suspension was filtered, and the precipitate was washed with deionized water until it was bromide-free. The washed precipitate was dried step-wise at 80, 90, 100, and 110 °C with 4 h dwell times. The final calcination was completed in an airflow atmosphere with a ramp rate of 2 °C/min at 550 °C for 6 h.

The functional material MCM-41@HNT with MCM-41, synthesized inside the halloysite nanotubes, was prepared according to the procedure described elsewhere [65]. Halloysite clay was pretreated via etching in hydrochloric acid (2 M) at 70 °C for 24 h. After filtering the suspension, the precipitate was washed and dried at 80 °C for 12 h. A charge of etched halloysite (5 g) was dispersed in a mixture of water (250 mL), hexadecyltrimethylammonium bromide (5 g), and 2-propanol (50 mL). After sonication for 60 min, the pH was adjusted to 10.5 using aqueous ammonia, and the suspension was stirred for 3 h. The gel was aged at room temperature for 24 h. Subsequent heating to 90 °C for 24 h led to the formation of a precipitate, which was washed, step-wise dried at 60, 80, 110, and 140 °C (with 2 h dwell times), and calcined with a ramp rate of 2 °C/min at 550 °C for 6 h.

3.3. Catalyst Preparation

The catalyst supports were prepared by mixing the corresponding functional material (HNT, MCM-41/HNT, MCM-41@HNT) with boehmite (20% wt.) using an aqueous peptizing agent with nitric acid (1 M) and polyethylene glycol (5% wt.). Pellets with a diameter of 2 mm were formed, dried out at room temperature for 24 h, step-wise at 80–110 °C, and calcined at 550 °C in an airflow atmosphere for 4 h. After crushing and sieving, the fraction 0.2–0.5 mm was used for impregnation.

The chromium was deposited by incipient wetness impregnation of the support with aqueous chromium (III) nitrate for 8 h with a subsequent dry-out at 100 °C for 5 h, and calcination at 550 °C in the air for 3 h. The moisture capacities of the supports were as follows: 0.51 g H₂O/g HNT, 1.05 g H₂O/g MCM-41/HNT, and 0.98 g H₂O/g MCM-41@HNT. The nominal chromium loading was 5 %wt.

3.4. Catalyst Characterization

The chromium content was determined using the X-ray fluorescence spectrometer ARL Perform'X (Thermo Fisher Scientific, Waltham, MA, USA) using the standardless UniQuant ED 6.30 software.

The low-temperature N₂ adsorption isotherms were measured with a Gemini VII 2390t (Micromeritics Instrument Corp., Norcross, GA, USA). Samples (0.5 g) were randomly selected from the same batch of catalyst that was used for the catalytic performance experiments. Sample outgassing was performed at 400 °C for 4 h in a vacuum. The specific surface area (S_{BET}) was estimated by using the Brunauer–Emmet–Teller (BET) method in the relative pressure range of 0.05–0.30. The pore size distribution was estimated by using the Barrett–Joyner–Halenda (BJH) model.

The phase composition of the catalysts was studied by X-ray diffraction (XRD) using the BrukerD2 (Billerica, MA, USA), Cu K α ($\lambda = 1.5406 \text{ \AA}$).

Transmission electron microscopy (TEM) was performed with the JEM-2100 (JEOL, Tokyo, Japan) with an accelerating voltage of 200 kV. The samples were crushed and dispersed in ethanol and then distributed onto 300-mesh Lacey copper TEM grids (Ted

Pella, Redding, CA, USA). The Lacey grids were chosen for their maximum clarity of TEM micrographs without a formvar background.

A temperature-programmed reduction with hydrogen (TPR-H₂) was conducted with the Autochem 2950HP (Micromeritics, Norcross, GA, USA) equipped with a quartz reactor and thermal conductivity detector. The reduction mixture contained 7% H₂-Ar (balance). The measurement conditions were as follows: flow rate of 30 mL/min; heating rate of 10 °C/min.

The acidity of the supports and catalysts was evaluated using the temperature-programmed desorption of ammonia (TPD-NH₃) on the Autochem 2950HP (Micromeritics, Norcross, GA, USA) equipped with a quartz reactor and thermal conductivity detector. NH₃ adsorption was carried out at 60 °C for 30 min. Physically adsorbed ammonia was removed in a nitrogen flow at 100 °C for 30 min. The TPD-NH₃ analysis was performed upon heating the sample from 100 to 700 °C with a temperature ramp of 10 °C/min.

Thermogravimetric analysis (TGA) of the spent catalysts was carried out on an STA 449F5 instrument (Netzsch, Waldkraiburg, Germany). A sample was placed in a corundum crucible and heated from 30 to 1000 °C with a heating rate of 10 K/min in an air stream (purge: 50 mL/min; protective (N₂): 20 mL/min). The final temperature was maintained for 2 h to ensure complete coke elimination. An empty Al₂O₃ crucible was applied as a reference.

3.5. Catalytic Tests

The catalytic experiments were performed in an isothermal fixed-bed quartz reactor at atmospheric pressure. Before the catalysts' activity evaluation, blank experiments with quartz beds at 550–600 °C were conducted, and the propane conversion did not exceed 5.5%. The main products were C1-C2 hydrocarbons. The propane and CO₂ flow rates were controlled independently by mass-flow controllers from Bronkhorst. A catalyst sample (1 g) was mixed with quartz beds (2 g). The propane flow rate was 10 mL/min, and the molar ratio of CO₂/C₃H₈ was equal to 2. Before each test, the catalysts were regenerated at 650 °C for 1 h in an airflow atmosphere.

On-line gas chromatography of the feedstock and products was performed using the Chromos GC-1000 (Chromos Engineering, Dzerzhinsk, Russia) equipped with a capillary column Valco PLOT VP-Alumina Na₂SO₄ (50 m × 0.53 mm × 10 μm) and flame ionization detector. The deviation between parallel experiments did not exceed 5%.

The conversion of propane ($X_{C_3H_8}$) was calculated as

$$X_{C_3H_8} = \frac{C_{C_3H_8}^{in} - C_{C_3H_8}^{out}}{C_{C_3H_8}^{in}}, \quad (1)$$

and the selectivity to propylene ($S_{C_3H_6}$) was according to the following equation:

$$S_{C_3H_6} = \frac{C_{C_3H_6}^{out} - C_{C_3H_6}^{in}}{C_{C_3H_8}^{in} - C_{C_3H_8}^{out}}, \quad (2)$$

where C_i^{in} and C_i^{out} are the reactor inlet and outlet concentration.

The space-time yield was calculated as follows:

$$STY = \frac{F \cdot C_{C_3H_8}^{in} \cdot X_{C_3H_8} \cdot S_{C_3H_6}}{m_{cat}}, \quad (3)$$

where F is the molar flow rate of the feedstock.

The rate of the propane conversion was estimated as follows:

$$r_{C_3H_8} = \frac{F \cdot C_{C_3H_8}^{in} \cdot X_{C_3H_8}}{m_{cat}}, \quad (4)$$

where the above-mentioned designations are used.

4. Conclusions

Three types of chromia catalysts for propane oxidative dehydrogenation with carbon dioxide were prepared: supported on halloysite nanotubes; MCM-41, templated around halloysite nanotubes; or MCM-41, embedded in halloysite nanotubes. The silica of MCM-41-type synthesis around or inside halloysite nanotubes improves the textural properties of halloysite and the thermal stability of MCM-41. Compared to pristine halloysite nanotubes, MCM-41-decorated supports show significantly higher specific surface areas and smaller average pore diameters. The effect of specific surface area increases is especially pronounced for MCM-41/HNT. The catalyst based on MCM-41 around nanotubes shows the best performance, which could be related to the highest BET surface area (558 m²/g) and uniform distribution of chromia. The space–time yield exceeds 7 mol C₃H₈/kg cat/h (at 700 °C).

The catalytic performance of the obtained composites shows that a high surface area and thermal stability are essential for CO₂-assisted propane dehydrogenation catalysts. Furthermore, the morphology of the catalyst particles plays an important role: the catalysts with similar composition and chromia content (namely, Cr/MCM-41/HNT and Cr/MCM-41@HNT) demonstrate remarkably different performances. The best of the tested catalysts, Cr/MCM-41/HNT, combines easily available MCM-41-type surface and larger pores that are formed by the halloysite nanotubes. Halloysite nanotubes are available in thousands of tons worldwide and could be easily scaled up for industrial applications.

Further developments for better propane dehydrogenation may involve the nano-architectural approach, namely, the catalysts combining macropores and ordered mesoporous materials for the maximum availability of chromia-active centers. It is worth noting that the performance of the chromia-based catalysts can also be tailored by promoting them with alkali. These improvements will help to close the “propylene gap” and utilize industrial carbon dioxide, thus facilitating the transition to greener petrochemical processes.

Author Contributions: Conceptualization, D.M., A.G. and V.V.; methodology, A.N.; software, E.I.; validation, A.N. and D.M.; formal analysis, H.W.; investigation, E.S. and M.R.; resources, V.V.; data curation, A.G.; writing—original draft preparation, D.M. and A.N.; writing—review and editing, D.M., A.N. and A.G.; visualization, M.R., D.M. and A.N.; supervision, A.G.; project administration, A.N.; funding acquisition, V.V. and H.W. All authors have read and agreed to the published version of the manuscript.

Funding: The study was supported by the Ministry of Science and Higher Education of the Russian Federation (agreement no. 075-15-2021-1386; code 13.2251.21.0100). The studies, performed at Northwestern Polytechnic University, were supported within the framework of the National Key Program of Research and Development of China (project no. 2021YFE0115100).

Data Availability Statement: Data is contained within the article. Additional data may be provided on request.

Conflicts of Interest: The authors declare no conflict of interest.

References

1. Eisele, P.; Killpack, R. Propene. In *Ullmann's Encyclopedia of Industrial Chemistry*; Wiley-VCH Verlag GmbH & Co. KGaA: Weinheim, Germany, 2011; Volume 16, pp. 75–81.
2. Searles, K.; Chan, K.W.; Mendes Burak, J.A.; Zemlyanov, D.; Safonova, O.; Copéret, C. Highly Productive Propane Dehydrogenation Catalyst Using Silica-Supported Ga-Pt Nanoparticles Generated from Single-Sites. *J. Am. Chem. Soc.* **2018**, *140*, 11674–11679. [[CrossRef](#)] [[PubMed](#)]
3. Carter, J.H.; Bere, T.; Pitchers, J.R.; Hewes, D.G.; Vandegheuchte, B.D.; Kiely, C.J.; Taylor, S.H.; Hutchings, G.J. Direct and Oxidative Dehydrogenation of Propane: From Catalyst Design to Industrial Application. *Green Chem.* **2021**, *23*, 9747–9799. [[CrossRef](#)]
4. Monai, M.; Gambino, M.; Wannakao, S.; Weckhuysen, B.M. Propane to Olefins Tandem Catalysis: A Selective Route towards Light Olefins Production. *Chem. Soc. Rev.* **2021**, *50*, 11503–11529. [[CrossRef](#)] [[PubMed](#)]
5. Akah, A.; Al-Ghrami, M. Maximizing Propylene Production via FCC Technology. *Appl. Petrochem. Res.* **2015**, *5*, 377–392. [[CrossRef](#)]

6. Sattler, J.J.H.B.; Ruiz-Martinez, J.; Santillan-Jimenez, E.; Weckhuysen, B.M. Catalytic Dehydrogenation of Light Alkanes on Metals and Metal Oxides. *Chem. Rev.* **2014**, *114*, 10613–10653. [[CrossRef](#)] [[PubMed](#)]
7. Chen, S.; Chang, X.; Sun, G.; Zhang, T.; Xu, Y.; Wang, Y.; Pei, C.; Gong, J. Propane Dehydrogenation: Catalyst Development, New Chemistry, and Emerging Technologies. *Chem. Soc. Rev.* **2021**, *50*, 3315–3354. [[CrossRef](#)]
8. Zimmermann, H.; Walzl, R. Ethylene. In *Ullmann's Encyclopedia of Industrial Chemistry*; Wiley-VCH Verlag GmbH & Co. KGaA: Weinheim, Germany, 2000; Volume 13, pp. 465–529.
9. Melnikov, D.P.; Novikov, A.A.; Glotov, A.P.; Reshetina, M.V.; Smirnova, E.M.; Wang, H.Q.; Vinokurov, V.A. Dehydrogenation of Light Alkanes (A Review). *Pet. Chem.* **2022**, *62*, 1027–1046. [[CrossRef](#)]
10. Caspary, K.J.; Gehrke, H.; Heinritz-Adrian, M.; Schwefer, M. Dehydrogenation of Alkanes. In *Handbook of Heterogeneous Catalysis*; Wiley-VCH Verlag GmbH & Co. KGaA: Weinheim, Germany, 2008; pp. 3206–3229.
11. Atanga, M.A.; Rezaei, F.; Jawad, A.; Fitch, M.; Rowanghi, A.A. Oxidative Dehydrogenation of Propane to Propylene with Carbon Dioxide. *Appl. Catal. B Environ.* **2018**, *220*, 429–445. [[CrossRef](#)]
12. Otroshchenko, T.; Jiang, G.; Kondratenko, V.A.; Rodemerck, U.; Kondratenko, E.V. Current Status and Perspectives in Oxidative, Non-Oxidative and CO₂-Mediated Dehydrogenation of Propane and Isobutane over Metal Oxide Catalysts. *Chem. Soc. Rev.* **2021**, *50*, 473–527. [[CrossRef](#)]
13. Rigamonti, M.G.; Shah, M.; Gambu, T.G.; Saeys, M.; Dusselier, M. Reshaping the Role of CO₂ in Propane Dehydrogenation: From Waste Gas to Platform Chemical. *ACS Catal.* **2022**, *12*, 9339–9358. [[CrossRef](#)]
14. Huš, M.; Kopač, D.; Bajec, D.; Likozar, B. Effect of Surface Oxidation on Oxidative Propane Dehydrogenation over Chromia: An Ab Initio Multiscale Kinetic Study. *ACS Catal.* **2021**, *11*, 11233–11247. [[CrossRef](#)] [[PubMed](#)]
15. Routray, K.; Reddy, K.R.S.K.; Deo, G. Oxidative Dehydrogenation of Propane on V₂O₅/Al₂O₃ and V₂O₅/TiO₂ Catalysts: Understanding the Effect of Support by Parameter Estimation. *Appl. Catal. A Gen.* **2004**, *265*, 103–113. [[CrossRef](#)]
16. Carrero, C.A.; Schloegl, R.; Wachs, I.E.; Schomaecker, R. Critical Literature Review of the Kinetics for the Oxidative Dehydrogenation of Propane over Well-Defined Supported Vanadium Oxide Catalysts. *ACS Catal.* **2014**, *4*, 3357–3380. [[CrossRef](#)]
17. Tedeeva, M.A.; Kustov, A.L.; Pribytkov, P.V.; Leonov, A.V.; Dunaev, S.F. Dehydrogenation of Propane with CO₂ on Supported CrO_x/SiO₂ Catalysts. *Russ. J. Phys. Chem. A* **2018**, *92*, 2403–2407. [[CrossRef](#)]
18. Chernyak, S.A.; Kustov, A.L.; Stolbov, D.N.; Tedeeva, M.A.; Isaikina, O.Y.; Maslakov, K.I.; Usol'tseva, N.V.; Savilov, S.V. Chromium Catalysts Supported on Carbon Nanotubes and Graphene Nanoflakes for CO₂-Assisted Oxidative Dehydrogenation of Propane. *Appl. Surf. Sci.* **2022**, *578*, 152099. [[CrossRef](#)]
19. Tedeeva, M.A.; Kustov, A.L.; Pribytkov, P.V.; Evdokimenko, N.D.; Sarkar, B.; Kustov, L.M. Dehydrogenation of Propane in the Presence of CO₂ on Cr(3%)/SiO₂ Catalyst under Supercritical Conditions. *Mendeleev Commun.* **2020**, *30*, 195–197. [[CrossRef](#)]
20. Nakagawa, K.; Okamura, M.; Ikenaga, N.; Suzuki, T.; Kobayashi, T. Dehydrogenation of Ethane over Gallium Oxide in the Presence of Carbon Dioxide. *Chem. Commun.* **1998**, *3*, 1025–1026. [[CrossRef](#)]
21. Tedeeva, M.A.; Kustov, A.L.; Pribytkov, P.V.; Strekalova, A.A.; Kalmykov, K.B.; Dunaev, S.F.; Kustov, L.M. Dehydrogenation of Propane in the Presence of CO₂ on Supported Monometallic MO_y/SiO₂ and CrO_xMO_y/SiO₂ (M = Fe, Co, and Ni) Bimetallic Catalysts. *Russ. J. Phys. Chem. A* **2021**, *95*, 55–62. [[CrossRef](#)]
22. Tedeeva, M.A.; Kustov, A.L.; Pribytkov, P.V.; Kapustin, G.I.; Leonov, A.V.; Tkachenko, O.P.; Tursunov, O.B.; Evdokimenko, N.D.; Kustov, L.M. Dehydrogenation of Propane in the Presence of CO₂ on GaO_x/SiO₂ Catalyst: Influence of the Texture Characteristics of the Support. *Fuel* **2022**, *313*, 122698. [[CrossRef](#)]
23. Mitchell, P.C.H.; Wass, S.A. Propane Dehydrogenation over Molybdenum Hydrotalcite Catalysts. *Appl. Catal. A Gen.* **2002**, *225*, 153–165. [[CrossRef](#)]
24. Koc, S.N.; Dayioglu, K.; Ozdemir, H. Oxidative Dehydrogenation of Propane with K-MoO₃/MgAl₂O₄ Catalysts. *J. Chem. Sci.* **2016**, *128*, 67–71. [[CrossRef](#)]
25. Castro-Fernández, P.; Mance, D.; Liu, C.; Moroz, I.B.; Abdala, P.M.; Pidko, E.A.; Copéret, C.; Fedorov, A.; Müller, C.R. Propane Dehydrogenation on Ga₂O₃-Based Catalysts: Contrasting Performance with Coordination Environment and Acidity of Surface Sites. *ACS Catal.* **2021**, *11*, 907–924. [[CrossRef](#)]
26. Ascoop, I.; Galvita, V.V.; Alexopoulos, K.; Reyniers, M.-F.; Van Der Voort, P.; Bliznuk, V.; Marin, G.B. The Role of CO₂ in the Dehydrogenation of Propane over WO_x-VO_x/SiO₂. *J. Catal.* **2016**, *335*, 1–10. [[CrossRef](#)]
27. Searles, K.; Siddiqi, G.; Safonova, O.V.; Copéret, C. Silica-Supported Isolated Gallium Sites as Highly Active, Selective and Stable Propane Dehydrogenation Catalysts. *Chem. Sci.* **2017**, *8*, 2661–2666. [[CrossRef](#)] [[PubMed](#)]
28. Nazimov, D.A.; Klimov, O.V.; Danilova, I.G.; Trukhan, S.N.; Saiko, A.V.; Cherepanova, S.V.; Chesalov, Y.A.; Martyanov, O.N.; Noskov, A.S. Effect of Alumina Polymorph on the Dehydrogenation Activity of Supported Chromia/Alumina Catalysts. *J. Catal.* **2020**, *391*, 35–47. [[CrossRef](#)]
29. Michorczyk, P.; Pietrzyk, P.; Ogonowski, J. Preparation and Characterization of SBA-1-Supported Chromium Oxide Catalysts for CO₂ Assisted Dehydrogenation of Propane. *Microporous Mesoporous Mater.* **2012**, *161*, 56–66. [[CrossRef](#)]
30. Mitran, G.; Ahmed, R.; Iro, E.; Hajimirzaee, S.; Hodgson, S.; Urdá, A.; Olea, M.; Marcu, I.C. Propane Oxidative Dehydrogenation over VO_x/SBA-15 Catalysts. *Catal. Today* **2018**, *306*, 260–267. [[CrossRef](#)]
31. Asghari, S.; Haghighi, M.; Taghavinezhad, P. Plasma-Enhanced Dispersion of Cr₂O₃ over Ceria-Doped MCM-41 Nanostructured Catalyst Used in CO₂ Oxidative Dehydrogenation of Ethane to Ethylene. *Microporous Mesoporous Mater.* **2019**, *279*, 165–177. [[CrossRef](#)]

32. Liu, Q.; Li, J.; Zhao, Z.; Gao, M.; Kong, L.; Liu, J.; Wei, Y. Design, Synthesis and Catalytic Performance of Vanadium-Incorporated Mesoporous Silica KIT-6 Catalysts for the Oxidative Dehydrogenation of Propane to Propylene. *Catal. Sci. Technol.* **2016**, *6*, 5927–5941. [[CrossRef](#)]
33. Zhang, F.; Wu, R.; Yue, Y.; Yang, W.; Gu, S.; Miao, C.; Hua, W.; Gao, Z. Chromium Oxide Supported on ZSM-5 as a Novel Efficient Catalyst for Dehydrogenation of Propane with CO₂. *Microporous Mesoporous Mater.* **2011**, *145*, 194–199. [[CrossRef](#)]
34. Guo, H.; He, H.; Miao, C.; Hua, W.; Yue, Y.; Gao, Z. CO₂ Assisted Ethane Dehydrogenation over Co-Exchanged ZSM-5 and ZSM-11 Zeolites: Effect of Al Spatial Distribution. *Appl. Catal. A Gen.* **2022**, *635*, 118569. [[CrossRef](#)]
35. Yu, J.; Shi, J.-L.; Wang, L.-Z.; Ruan, M.-L.; Yan, D.-S. Preparation of High Thermal Stability MCM-41 in the Low Surfactant/Silicon Molar Ratio Synthesis Systems. *Mater. Lett.* **2001**, *48*, 112–116. [[CrossRef](#)]
36. Chakraborty, B.; Viswanathan, B. Surface Acidity of MCM-41 by in Situ IR Studies of Pyridine Adsorption. *Catal. Today* **1999**, *49*, 253–260. [[CrossRef](#)]
37. Orlyk, S.; Kyriienko, P.; Kapran, A.; Chedryk, V.; Balakin, D.; Gurgul, J.; Zimowska, M.; Millot, Y.; Dzwigaj, S. CO₂-Assisted Dehydrogenation of Propane to Propene over Zn-BEA Zeolites: Impact of Acid–Base Characteristics on Catalytic Performance. *Catalysts* **2023**, *13*, 681. [[CrossRef](#)]
38. Singh, B.; Na, J.; Konarova, M.; Wakihara, T.; Yamauchi, Y.; Salomon, C.; Gawande, M.B. Functional Mesoporous Silica Nanomaterials for Catalysis and Environmental Applications. *Bull. Chem. Soc. Jpn.* **2020**, *93*, 1459–1496. [[CrossRef](#)]
39. Giraldo, L.F.; López, B.L.; Pérez, L.; Urrego, S.; Sierra, L.; Mesa, M. Mesoporous Silica Applications. *Macromol. Symp.* **2007**, *258*, 129–141. [[CrossRef](#)]
40. Zhang, X.; Yue, Y.; Gao, Z. Chromium Oxide Supported on Mesoporous SBA-15 as Propane Dehydrogenation and Oxidative Dehydrogenation Catalysts. *Catal. Lett.* **2002**, *83*, 19–25. [[CrossRef](#)]
41. Chen, Q.; Deng, L.; Wu, Z.; Wang, F.; Jiang, X. Mesoporous Silica SBA-15 Supported Pt-Ga Nanoalloys as an Active and Stable Catalyst for Propane Dehydrogenation. *Ind. Eng. Chem. Res.* **2022**, *61*, 7799–7809. [[CrossRef](#)]
42. Al-Awadi, A.S.; El-Toni, A.M.; Alhoshan, M.; Khan, A.; Labis, J.P.; Al-Fatesh, A.; Abasaeed, A.E.; Al-Zahrani, S.M. Impact of Precursor Sequence of Addition for One-Pot Synthesis of Cr-MCM-41 Catalyst Nanoparticles to Enhance Ethane Oxidative Dehydrogenation with Carbon Dioxide. *Ceram. Int.* **2019**, *45*, 1125–1134. [[CrossRef](#)]
43. Baek, J.; Yun, H.J.; Yun, D.; Choi, Y.; Yi, J. Preparation of Highly Dispersed Chromium Oxide Catalysts Supported on Mesoporous Silica for the Oxidative Dehydrogenation of Propane Using CO₂: Insight into the Nature of Catalytically Active Chromium Sites. *ACS Catal.* **2012**, *2*, 1893–1903. [[CrossRef](#)]
44. Michorczyk, P.; Ogonowski, J.; Niemczyk, M. Investigation of Catalytic Activity of CrSBA-1 Materials Obtained by Direct Method in the Dehydrogenation of Propane with CO₂. *Appl. Catal. A Gen.* **2010**, *374*, 142–149. [[CrossRef](#)]
45. Chernov, A.N.; Sobolev, V.I.; Gerasimov, E.Y.; Koltunov, K.Y. Propane Dehydrogenation on Co-N-C/SiO₂ Catalyst: The Role of Single-Atom Active Sites. *Catalysts* **2022**, *12*, 1262. [[CrossRef](#)]
46. Al-Awadi, A.S.; El-Toni, A.M.; Labis, J.P.; Khan, A.; Ghaitan, H.; Al-Zahrani, A.A.; Abasaeed, A.E.; Al-Zahrani, S.M. Mesoporous Organo-Silica Supported Chromium Oxide Catalyst for Oxidative Dehydrogenation of Ethane to Ethylene with CO₂. *Catalysts* **2021**, *11*, 642. [[CrossRef](#)]
47. Mashkin, M.Y.; Tedeeva, M.A.; Fedorova, A.A.; Fatula, E.R.; Egorov, A.V.; Dvoryak, S.V.; Maslakov, K.I.; Knotko, A.V.; Baranchikov, A.E.; Kapustin, G.I.; et al. Synthesis of Ce_xZr_{1-x}O₂/SiO₂ Supports for Chromium Oxide Catalysts of Oxidative Dehydrogenation of Propane with Carbon Dioxide. *J. Chem. Technol. Biotechnol.* **2023**, *98*, 1247–1259. [[CrossRef](#)]
48. Massaro, M.; Noto, R.; Riel, S. Halloysite Nanotubes: Smart Nanomaterials in Catalysis. *Catalysts* **2022**, *12*, 149. [[CrossRef](#)]
49. Glotov, A.; Stavitskaya, A.; Chudakov, Y.; Ivanov, E.; Huang, W.; Vinokurov, V.; Zolotukhina, A.; Maximov, A.; Karakhanov, E.; Lvov, Y. Mesoporous Metal Catalysts Templated on Clay Nanotubes. *Bull. Chem. Soc. Jpn.* **2019**, *92*, 61–69. [[CrossRef](#)]
50. Lisuzzo, L.; Cavallaro, G.; Milioto, S.; Lazzara, G. Halloysite Nanotubes Filled with MgO for Paper Reinforcement and Deacidification. *Appl. Clay Sci.* **2021**, *213*, 106231. [[CrossRef](#)]
51. Guo, W.; Xu, L.; Feng, P.; Gu, Y.; Shuai, C. In-Situ Growth of Silica Nano-Protrusions on Halloysite Nanotubes for Interfacial Reinforcement in Polymer/Halloysite Scaffolds. *Appl. Surf. Sci.* **2020**, *513*, 145772. [[CrossRef](#)]
52. Vinokurov, V.; Novikov, A.; Rodnova, V.; Anikushin, B.; Kotelev, M.; Ivanov, E.; Lvov, Y. Cellulose Nanofibrils and Tubular Halloysite as Enhanced Strength Gelation Agents. *Polymers* **2019**, *11*, 919. [[CrossRef](#)]
53. Rozza, R.; Armata, N.; Lazzara, G.; Parisi, F.; Ferrante, F. Halloysite Nanotubes and Metal Corrosion Inhibitors: A Computational and Experimental Study. *J. Phys. Chem. C* **2019**, *123*, 10451–10461. [[CrossRef](#)]
54. Novikov, A.A.; Sayfutdinova, A.R.; Gorbachevskii, M.V.; Filatova, S.V.; Filimonova, A.V.; Rodrigues-Filho, U.P.; Fu, Y.; Wang, W.; Wang, H.; Vinokurov, V.A.; et al. Natural Nanoclay-Based Silver–Phosphomolybdic Acid Composite with a Dual Antimicrobial Effect. *ACS Omega* **2022**, *7*, 6728–6736. [[CrossRef](#)] [[PubMed](#)]
55. Abdullayev, E.; Joshi, A.; Wei, W.; Zhao, Y.; Lvov, Y. Enlargement of Halloysite Clay Nanotube Lumen by Selective Etching of Aluminum Oxide. *ACS Nano* **2012**, *6*, 7216–7226. [[CrossRef](#)]
56. Jia, S.; Fan, M. Silanization of Heat-Treated Halloysite Nanotubes Using γ -Aminopropyltriethoxysilane. *Appl. Clay Sci.* **2019**, *180*, 105204. [[CrossRef](#)]
57. Vinokurov, V.A.; Stavitskaya, A.V.; Chudakov, Y.A.; Glotov, A.P.; Ivanov, E.V.; Gushchin, P.A.; Lvov, Y.M.; Maximov, A.L.; Muradov, A.V.; Karakhanov, E.A. Core-Shell Nanoarchitecture: Schiff-Base Assisted Synthesis of Ruthenium in Clay Nanotubes. *Pure Appl. Chem.* **2018**, *90*, 825–832. [[CrossRef](#)]

58. Glotov, A.; Vutolkina, A.; Pimerzin, A.; Vinokurov, V.; Lvov, Y. Clay Nanotube-Metal Core/Shell Catalysts for Hydroprocesses. *Chem. Soc. Rev.* **2021**, *50*, 9240–9277. [[CrossRef](#)]
59. Glotov, A.; Novikov, A.; Stavitskaya, A.; Nedolivko, V.; Kopitsyn, D.; Kuchierskaya, A.; Ivanov, E.; Stytsenko, V.; Vinokurov, V.; Lvov, Y. Nanoreactors Based on Hydrophobized Tubular Aluminosilicates Decorated with Ruthenium: Highly Active and Stable Catalysts for Aromatics Hydrogenation. *Catal. Today* **2021**, *378*, 33–42. [[CrossRef](#)]
60. Kokulnathan, T.; Wang, T.-J.; Ashok Kumar, E.; Ahmed, F. Construction of Nickel Cobalt-Layered Double Hydroxide/Functionalized-Halloysite Nanotubes Composite for Electrochemical Detection of Organophosphate Insecticide. *Chem. Eng. J.* **2022**, *433*, 133639. [[CrossRef](#)]
61. Rouster, P.; Dondelinger, M.; Galleni, M.; Nysten, B.; Jonas, A.M.; Glinel, K. Layer-by-Layer Assembly of Enzyme-Loaded Halloysite Nanotubes for the Fabrication of Highly Active Coatings. *Colloids Surf. B Biointerfaces* **2019**, *178*, 508–514. [[CrossRef](#)]
62. Glotov, A.; Vutolkina, A.; Pimerzin, A.; Nedolivko, V.; Zasyalov, G.; Stytsenko, V.; Karakhanov, E.; Vinokurov, V. Ruthenium Catalysts Templated on Mesoporous MCM-41 Type Silica and Natural Clay Nanotubes for Hydrogenation of Benzene to Cyclohexane. *Catalysts* **2020**, *10*, 537. [[CrossRef](#)]
63. Glotov, A.; Levshakov, N.; Stavitskaya, A.; Artemova, M.; Gushchin, P.; Ivanov, E.; Vinokurov, V.; Lvov, Y. Templated Self-Assembly of Ordered Mesoporous Silica on Clay Nanotubes. *Chem. Commun.* **2019**, *55*, 5507–5510. [[CrossRef](#)]
64. Karakhanov, E.; Maximov, A.; Zolotukhina, A.; Vinokurov, V.; Ivanov, E.; Glotov, A. Manganese and Cobalt Doped Hierarchical Mesoporous Halloysite-Based Catalysts for Selective Oxidation of p-Xylene to Terephthalic Acid. *Catalysts* **2020**, *10*, 7. [[CrossRef](#)]
65. Fu, L.; Yang, H.; Tang, A.; Hu, Y. Engineering a Tubular Mesoporous Silica Nanocontainer with Well-Preserved Clay Shell from Natural Halloysite. *Nano Res.* **2017**, *10*, 2782–2799. [[CrossRef](#)]
66. Glotov, A.; Levshakov, N.; Vutolkina, A.; Lysenko, S.; Karakhanov, E.; Vinokurov, V. Aluminosilicates Supported La-Containing Sulfur Reduction Additives for FCC Catalyst: Correlation between Activity, Support Structure and Acidity. *Catal. Today* **2019**, *329*, 135–141. [[CrossRef](#)]
67. Glotov, A.P.; Artemova, M.I.; Demikhova, N.R.; Smirnova, E.M.; Ivanov, E.V.; Gushchin, P.A.; Egazar'yants, S.V.; Vinokurov, V.A. A Study of Platinum Catalysts Based on Ordered Al-MCM-41 Aluminosilicate and Natural Halloysite Nanotubes in Xylene Isomerization. *Pet. Chem.* **2019**, *59*, 1226–1234. [[CrossRef](#)]
68. Han, Z.-F.; Xue, X.-L.; Wu, J.-M.; Lang, W.-Z.; Guo, Y.-J. Preparation and Catalytic Properties of Mesoporous NV-MCM-41 for Propane Oxidative Dehydrogenation in the Presence of CO₂. *Chin. J. Catal.* **2018**, *39*, 1099–1109. [[CrossRef](#)]
69. Michorczyk, P.; Ogonowski, J.; Kuśtrowski, P.; Chmielarz, L. Chromium Oxide Supported on MCM-41 as a Highly Active and Selective Catalyst for Dehydrogenation of Propane with CO₂. *Appl. Catal. A Gen.* **2008**, *349*, 62–69. [[CrossRef](#)]
70. Wang, Y.; Ohishi, Y.; Shishido, T.; Zhang, Q.; Yang, W.; Guo, Q.; Wan, H.; Takehira, K. Characterizations and Catalytic Properties of Cr-MCM-41 Prepared by Direct Hydrothermal Synthesis and Template-Ion Exchange. *J. Catal.* **2003**, *220*, 347–357. [[CrossRef](#)]
71. Zaki, M.I.; Fouad, N.E.; Bond, G.C.; Tahir, S.F. Temperature-Programmed Reduction of Calcined Chromia-Coated Alumina and Silica Catalysts: Probing Chromium (VI)-Oxygen Species. *Thermochim. Acta* **1996**, *285*, 167–179. [[CrossRef](#)]
72. Cabrera, F.; Ardisson, D.; Gorris, O.F. Dehydrogenation of Propane on Chromia/Alumina Catalysts Promoted by Tin. *Catal. Today* **2008**, *133–135*, 800–804. [[CrossRef](#)]
73. Dinse, A.; Khennache, S.; Frank, B.; Hess, C.; Herbert, R.; Wrabetz, S.; Schlögl, R.; Schomäcker, R. Oxidative Dehydrogenation of Propane on Silica (SBA-15) Supported Vanadia Catalysts: A Kinetic Investigation. *J. Mol. Catal. A Chem.* **2009**, *307*, 43–50. [[CrossRef](#)]
74. Gaydhankar, T.R.; Samuel, V.; Jha, R.K.; Kumar, R.; Joshi, P.N. Room Temperature Synthesis of Si-MCM-41 Using Polymeric Version of Ethyl Silicate as a Source of Silica. *Mater. Res. Bull.* **2007**, *42*, 1473–1484. [[CrossRef](#)]

Disclaimer/Publisher's Note: The statements, opinions and data contained in all publications are solely those of the individual author(s) and contributor(s) and not of MDPI and/or the editor(s). MDPI and/or the editor(s) disclaim responsibility for any injury to people or property resulting from any ideas, methods, instructions or products referred to in the content.